Supporting Information

Over-Etching Constructing V_2O_3-VC/C Directly from MAX Phase for Lithium-Sulfur Batteries

Mengjie Zhang,‡ Maoqiang Shen,‡ Yang Liu*, Hong Xiao*, Rui Wan, Linrui Hou, Changzhou Yuan*

School of Materials Science & Engineering, University of Jinan, Jinan, 250022, P. R. China.

E-mail: mse_yuancz@ujn.edu.cn; ayuancz@163.com

‡ These authors have contributed equally to this work.

1. Experimental section

1.1. Chemicals and Materials

V_2AlC MAX was purchased from Yiyi Technology. S powder, 1-methyl-2-pyrrolidone (NMP), and ketjen black (KB) were purchased from Sinopharm Chemical Reagent Co., LTD. 1, 2-dimethoxyethane (DME), 1, 3-dimethoxyethane (DOL), Li_2S, and conventional electrolyte LS-009 (DOL/DME solution (1 : 1, volume ratio) containing 1 M LiTFSI and 2% $LiNO_3$) were purchased from DoDoChem. Carbon black and polyvinylidene fluoride (PVDF) were purchased from Guangdong Kangde New Energy Technology Co., LTD. All the chemical reagents here are used directly and have not been purified.

1.2. Material synthesis

Synthesis of V_2O_3-VC/C nanosheets: 1 g of PVDF was placed at the front of the corundum boat, while 0.2 g of V_2AlC MAX was evenly distributed at the rear. It was then placed in a corundum tube, heated at a rate of 5 ºC min^{-1} to 700 ºC and maintained for 0.5 h under the Ar atmosphere. After natural cooling to room temperature, the product V_2AlC-PVDF-700 at the rear of the corundum boat was collected. Subsequently, 0.2 g of V_2AlC-PVDF-700 was fully dispersed into 40 mL of 1 M NaOH solution, sealed within a polytetrafluoroethylene reactor, and reacted at 120 ºC for 2 h to remove AlF_3. Finally, the V_2O_3-VC/C-700 nanosheets were obtained by washing and filtering with deionized water, and then drying at 60 ºC for 12 h. With all other conditions unchanged, the etching temperature was adjusted to 800 ºC to obtain V_2O_3-VC/C-800 nanosheets.

Preparation of V_2C MXene: 1 g of PVDF was placed at the front of the corundum boat, and 0.2 g of V_2AlC MAX was evenly distributed at the rear of the same corundum boat. Then, it was sealed in an Ar protected corundum tube, and heated at a rate of 5 ºC

min^{-1} to 600 ºC and maintained for 0.5 h, collect the product V_2AlC-PVDF-6 from the rear. Subsequently, 0.2 g of V_2AlC-PVDF-600 was dispersed into 40 mL of 1 M NaOH solution, sealed in a polytetrafluoroethylene reactor, and heat to 120 ºC for 2 h to remove AlF_3. After washing and filtration, the V_2C MXene was obtained by vacuum drying at 60 ºC for 12 h.

Fabrication of the Modified Separators: The synthesized V_2O_3-VC/C-700, V_2O_3-VC/C-800 or V_2C were mixed, respectively, with conductive carbon black and PVDF in NMP to form a slurry with a ratio of 7 : 2 : 1. The uniformly slurry was coated onto the surface of the Celgard 2500 polypropylene (PP) separator, and then vacuum dried at 60 ºC for 12 h to evaporate the NMP solvent.

Preparation of S Cathodes: KB/S composite was prepared by the melt-diffusion method. Typically, a uniform mixture of KB and sulfur (mass ratio of 1 : 3) is transferred into an autoclave lined with polytetrafluoroethylene under an Ar atmosphere. Subsequently, it was heated at 155 ºC for 12 h to obtain the KB/S composite. Finally, the KB/S composite, PVDF, and carbon black were mixed homogeneously in the mass ratio of 8 : 1 : 1, and dispersed in NMP to form a slurry. The homogeneous slurry was coated on the Al foil and dried under vacuum at 60 ºC for 12 h, then cut into discs with a diameter of 12 mm to get S cathodes. For each cathode, the sulfur loading was controlled in the range of 0.9 – 1.2 mg cm^{-2}. According to the same method, high-loading cathodes with sulfur loading of 3.4 mg cm^{-2} were obtained by using carbon paper as the current collector.

LiPSs Permeation Test: Li_2S_6 solution (5 mM) was prepared by dispersing sulfur and Li_2S with a molar ratio of 5 : 1 in a mixed solvent of DME and DOL (1 : 1, volume ratio) under stirring at 60 ºC for 12 h. Normally, H-type electrolytic cells were used for the Li_2S_6 permeation test. The modified separator was cut into discs with a diameter of

18 mm and fixed in the middle of the H-type electrolytic cells. One said of the H-type electrolytic cell was injected with Li_2S_6 solution (5 mM, 20 mL), while the other said was filled with a mixture of DOL and DME (1 : 1, volume ratio, 20 mL). The color changes of Li_2S_6 permeation test were observed and recorded in real time to analyze the inhibition effect for different modified materials on the shuttle effect of soluble LiPSs.

Visualized Adsorption of Li_2S_6: Equal mass (40 mg) of modified materials were added separately to 3 mM Li_2S_6 solution (4 mL) and left to stand for 12 h, then the adsorbed supernatant was analyzed by UV spectroscopy.

Symmetric Cell Assembly and Kinetic Evaluation of LiPSs Conversion: 0.2 M Li_2S_6 based electrolyte was prepared by dispersing sulfur and Li_2S in conventional electrolyte LS-009 at a molar ratio of 5 : 1. Electrodes for symmetric cells were prepared by dispersing the active materials in ethanol and coating them on the carbon paper. Two equivalent electrodes were used as working and counter electrodes with a loading of 1 mg cm^{-2} and an electrolyte of 0.2 M Li_2S_6 (25 μL). The cyclic voltammetry (CV) test was performed for the symmetric cells at the scan rate of 1mV s^{-1} in the voltage range of -1.0 – 1.0 V.

Nucleation and Decomposition Measurements of Li_2S: 0.2 M Li_2S_8 based electrolyte was prepared by adding S and Li_2S with a molar ratio of 7:1 in the blank electrolyte. For battery assembly, the equal masses of V_2O_3-VC/C-800, V_2O_3-VC/C-700 or V_2C coating on the carbon paper (mass loading of 1.5 mg cm^{-2}) as the cathode, and Li foil as the anode, with 25 μL of Li_2S_8 electrolyte drops on the cathode side, and 25 μL of conventional electrolyte LS-009 drops on the anode side.

For nucleation text, the battery was discharged at a current of 0.112 mA to 2.10 V, and then discharged at a constant potential of 2.09 V until the current fell below 0.01

mA. The nucleation capacity of Li_2S could be calculated by Faraday's law from the integral area of the curve.

For decomposition text, the battery was discharged to 1.80 V at 0.10 mA, and then further discharged to 1.70 V at 0.01 mA to ensure that LiPSs were fully converted to solid Li_2S on the catalyst surface. After that, the battery was charged at a constant potential of 2.35 V until the current fell below 10^{-5} A.

Ionic conductivity calculation: The ionic conductivity (σ) and resistance (R_f) of the commercial PP separator and modified separators were investigated using an electrochemical workstation in the AC mode, with a frequency range of 100 kHz to 0.01 Hz and an amplitude of 10 mV. The ionic conductivity of the separators was tested in SS/PP or modified-PP/SS cells and calculated using the corresponding formula[1].

$$\sigma = \frac{L}{R_b \times A} \qquad \text{eq.1}$$

where L, A, and R_b were the thickness (cm) of separator, the effective area of separator (cm^2) and bulk resistance (Ω), respectively

1.3. Material characterization

The micro-morphologies of V_2O_3-VC/C-700, V_2O_3-VC/C-800 and V_2C were investigated by field emission scanning electron microscopy (FESEM, JEOL-6300F) and transmission electron microscopy (TEM, JEOL JEM-2100). Phase information of samples was detected by X-ray diffraction (XRD, Rigaku Uitima IV) and Raman microscope with a 532 nm laser excitation (InVia Reflex). X-ray photoelectron spectroscopy (XPS, PHI VersaProbe III) was conducted to study the chemical compositions and functional groups of the samples. The specific surface area and pore size distribution were determined *via* the Brunauer-Emmett-Teller method, with N_2 adsorption-desorption tests conducted at 77 K (Quantachrome, USA).

1.4. Electrochemical measurements

All the electrochemical measurements were tested in CR2032-type coin cells. The coin cells were assembled in an Ar-filled glovebox with KB/S electrode as cathode, Li metal as anode, and modified separator as separator. CV tests were carried out on the IVIUMSTAT workstation in the voltage window of 1.7 – 2.8 V. The galvanostatic charge/discharge plots were collected by the LAND battery-testing system (CT2001A). Electrochemical impedance spectroscopy (EIS) was performed in the frequency range of 0.01 Hz to 100 KHz.

1.5. Details of activation energy calculation

The CV of different modified separators was measured at a scan rate of 0.1mV s^{-1} at 298 K, as shown in Figure 6c. Among them, the relationship between electrode potential and activation energy is shown in eq. 2[2,3]:

$$E_a = E_a^0 + \alpha z F \varphi_{(\mathrm{Red})ir} \qquad \text{eq.2}$$

where E_a represented the activation energy of the reduction process, E_a^0 was the intrinsic activation energy, α was the symmetry factor, z was the number of transferred charges, and F is the Faraday constant. The irreversible $\varphi_{(\mathrm{Red})ir}$ in the reaction process is obtained through the peak potential of the redox peak on the CV curve.

The Tafel eq. 3:

$$\eta = \frac{RT}{\alpha z F} \ln j_0 - \frac{RT}{\alpha z F} \ln j \qquad \text{eq.3}$$

where η represented the overpotential, R was the gas constant, T was the absolute temperature, j_0 was the exchange current density, and j was the current density. This equation could be simplified to eq. 4:

$$\eta = a + b \ln j \qquad \text{eq.4}$$

Therefore, α and b correspond respectively to the intercept eq. 5 and slope eq. 6 of

the Tafel curve:

$$a = \frac{RT}{azF} lnj_0 \qquad \text{eq.5}$$

$$b = -\frac{RT}{azF} \qquad \text{eq.6}$$

Substituting the Tafel slope eq.6 into eq.2 yields a simplified eq.7:

$$E_a = E_a^0 - \frac{RT}{b} \varphi_{(Red)ir} \qquad \text{eq.7}$$

The reaction activation energies during the charging and discharging process were calculated by combining the Tafel curves shown in Figure S10 with the above equations.

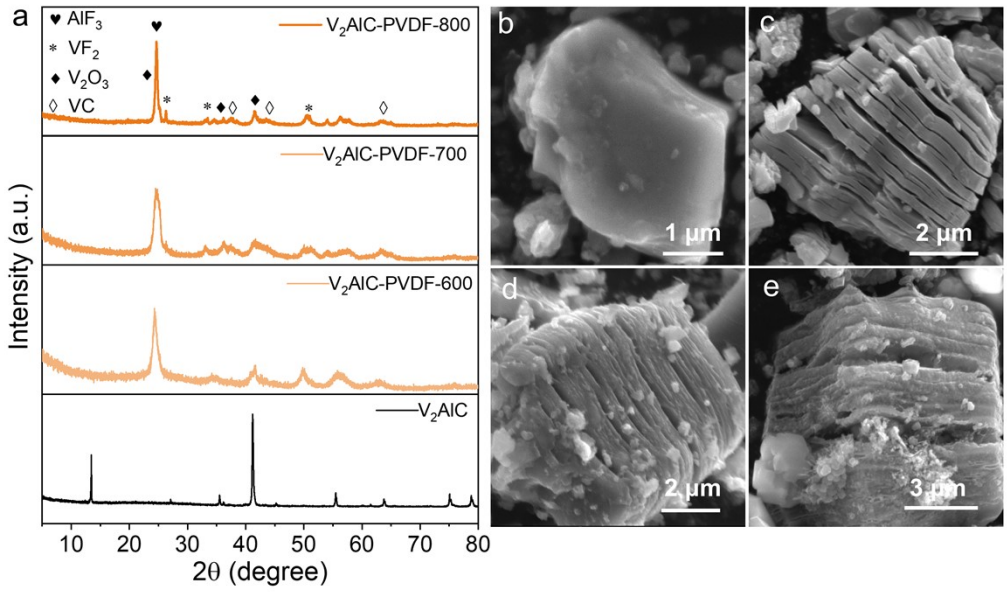

Fig. S1 (a) XRD patterns and SEM images of (b) V_2AlC, (c) V_2AlC-PVDF-600, (d) V_2AlC-PVDF-700 and (e) V_2AlC-PVDF-800.

As shown in the XRD pattern of Figure S1a, the intensity of the (002) peak at 13.47 º and the (103) peak at 41.28 º of V_2AlC has significantly declined after the gas-solid phase reaction, indicating that the selectively etching of Al layer in V_2AlC by HF gas. It is worth noting that the characteristic peaks corresponding to (012), (024), and (116) crystal plane of AlF_3 are observed at 24.7 º, 51.8 º, and 57.4 º, and the crystallinity of AlF_3 shows a significant strengthening with the increase of etching temperature. Furthermore, the formation of VF_2, VC, and V_2O_3 are observed in the patterns of both V_2AlC-PVDF-700 and V_2AlC-PVDF-800. This indicates that HF gas not only etches the Al layers but reacts with V to form VF_2, while simultaneously promoting structural transformation from V_2C to VC and inducing mild surface oxidation to generate V_2O_3. Such oxidation may be attributable to the presence of oxygen-containing functional groups within PVDF.[4,5]

As shown in Figure S1b, V_2AlC presents a typical dense block structure. After HF gas-solid phase etching, V_2AlC-PVDF-600 (Figure S1c), V_2AlC-PVDF-700 (Figure S1d), and V_2AlC-PVDF-800 (Figure S1e) all exhibit varying degrees of volume expansion, forming an accordion-like structure with nanoparticles adhering to the surface.

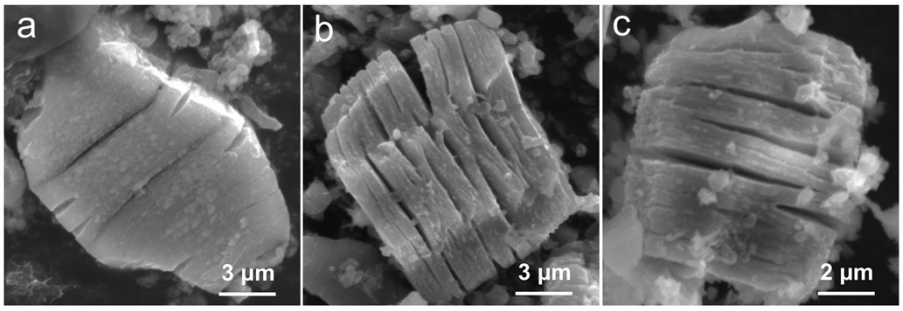

Fig. S2 SEM images of (a) V_2C, (b) V_2O_3-VC/C-700 and (C) V_2O_3-VC/C-800.

As shown in Fig. S2a, the V_2C MXene presents a highly smooth surface after NaOH treatment, with no AlF_3 observed, which demonstrates the efficient removal of fluoride by the alkali washing process. In addition, the surface nanoparticles of V_2O_3-VC/C-700 (Figure S2b) and V_2O_3-VC/C-800 (Figure S2c) decrease, showing more obvious gaps. It is worth noting that the accordion-like layered structure of MAX derivatives is not destroy during the NaOH treatment, but rather, its layered characteristics become more prominent.

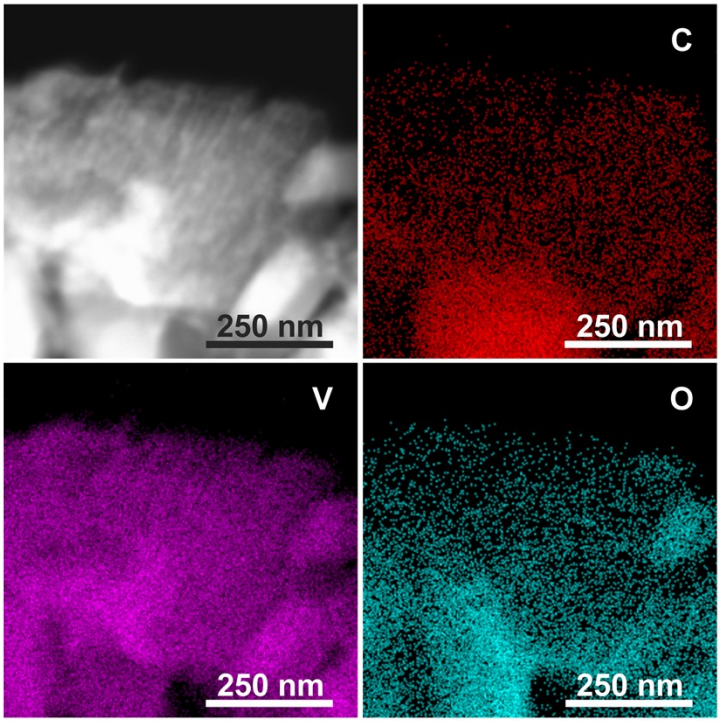

Fig. S3 EDX elemental mapping images of C, O, and V.

The energy-dispersive X-ray spectroscopy (EDS) elemental mapping in Fig. S3 reveals the uniform distribution of C, N, O, and V in V_2O_3-VC/C-700, further confirming the coexistence of V_2O_3 and VC derived from the over-etching of the MAX phase.

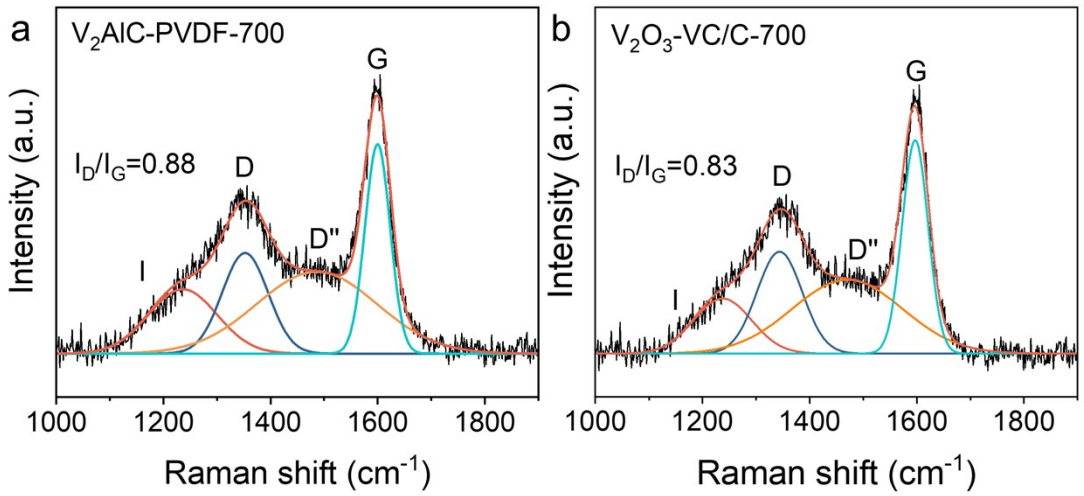

Fig. S4 Raman and fitting diagrams of (a) V_2AlC-PVDF-700 and (b) V_2O_3-VC/C-700.

As shown in Figure S4, two strong characteristic peaks can be observed at 1354 and 1596 cm^{-1}, belonging to the D and G bands of carbon, and the fitted peak area ratios (I_D/I_G) of the D and G bands are 0.88 and 0.83, respectively.

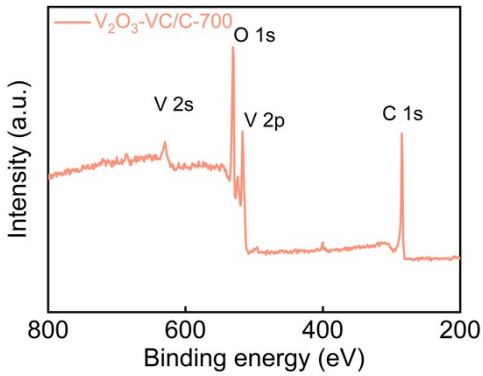

Fig. S5 The XPS spectrum of V_2O_3-VC/C-700.

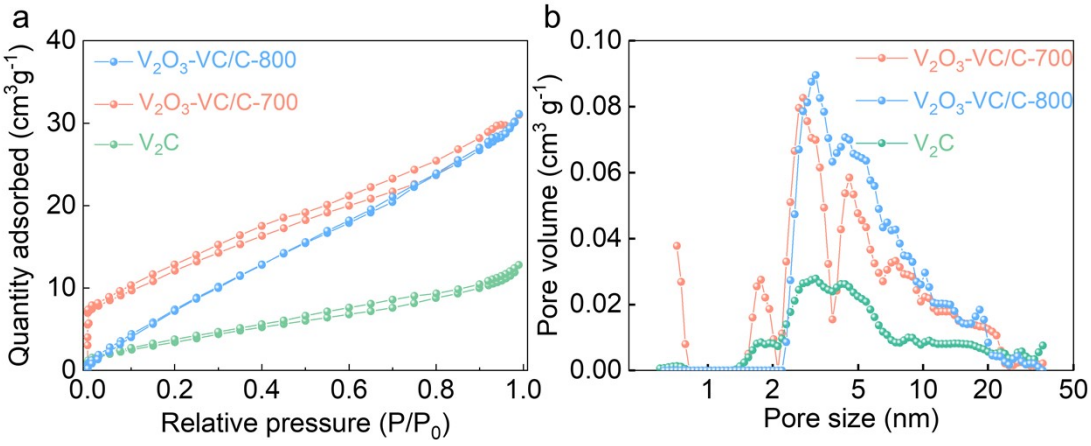

Fig. S6 (a) N_2 adsorption-desorption isothermal plots and (b) pore size distribution curves of V_2C, V_2O_3-VC/C-700 and V_2O_3-VC/C-800.

The specific surface area (SSA) and pore size of MAX derivatives obtained at different etching temperatures were analyzed by N_2 sorption experiments. V_2O_3-VC/C-700 possesses the largest SSA of 37.9 $cm^2\ g^{-1}$, higher than those of V_2C (24.4 $cm^2\ g^{-1}$) and V_2O_3-VC/C-800 (33.7 $cm^2\ g^{-1}$) (Table S1). The large SSA, pore volume and rich pore structure of V_2O_3-VC/C-700 not only facilitate the adsorption of LiPSs, but expose more catalytic active sites, accelerating the conversion of LiPSs.

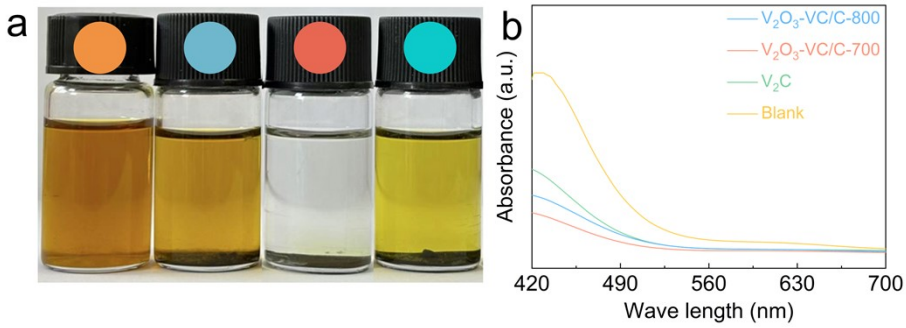

Fig. S7 (a) Digital photos of V_2C, V_2O_3-VC/C-700 and V_2O_3-VC/C-800 and (b) UV-vis spectra of the corresponding supernatant after Li_2S_6 adsorption experiment.

The adsorption capacity of V_2C, V_2O_3-VC/C-700 and V_2O_3-VC/C-800 for Li_2S_6 was investigated by Li_2S_6 adsorption experiments and UV spectra. Obviously, the color faded markedly in Li_2S_6 solution containing V_2O_3-VC/C-700, which reflects that V_2O_3-VC/C-700 has a good adsorption effect on LiPSs due to the strong chemisorption. In contrast, the adsorption of LiPSs by V_2C is poor, which is further confirmed by UV-vis spectroscopy.

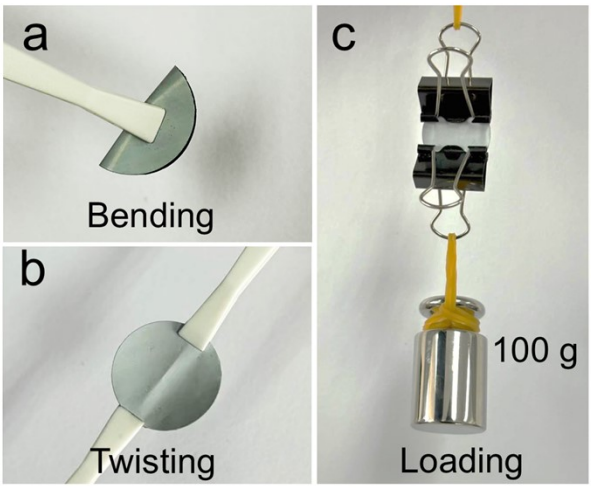

Fig. S8 (a) bending, (b) tensile and (c) loading tests of V_2O_3-VC/C-700/PP modified separator.

The coating in the V_2O_3-VC/C-700 modified separator (V_2O_3-VC/C-700/PP) remains intact without cracking or detachment after repeated folding and stretching, exhibiting its robust adhesion (Fig. S8, ESI).

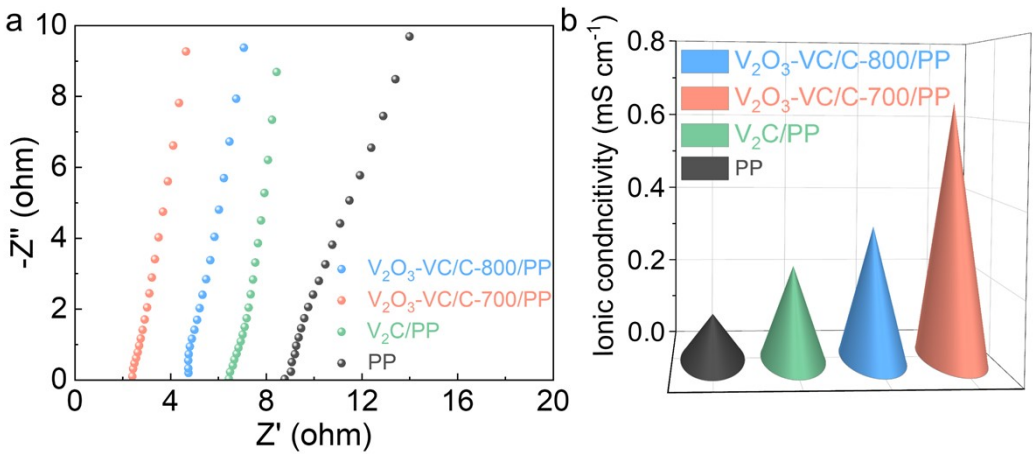

Fig. S9 (a) EIS plots and (b) Li^+ conductivities of the batteries with different separators.

Ionic conductivity is a key indicator for separator modification, which directly determines the ion transport efficiency, rate capability and safety of the battery system, and also serves as a critical quantitative basis for evaluating the effectiveness of modification strategies. The ionic conductivity of the V_2O_3-VC/C-700/PP coated separator is 0.6424 mS cm^{-1}, which is higher than those of V_2O_3-VC/C-800/PP (0.3313 mS cm^{-1}), V_2C/PP (0.232 mS cm^{-1}), and the commercial PP separator (0.112 mS cm^{-1}), as shown in Fig. S9. This further demonstrates that the V_2O_3-VC/C-700 coating layer endows PP with superior ion transport kinetics.

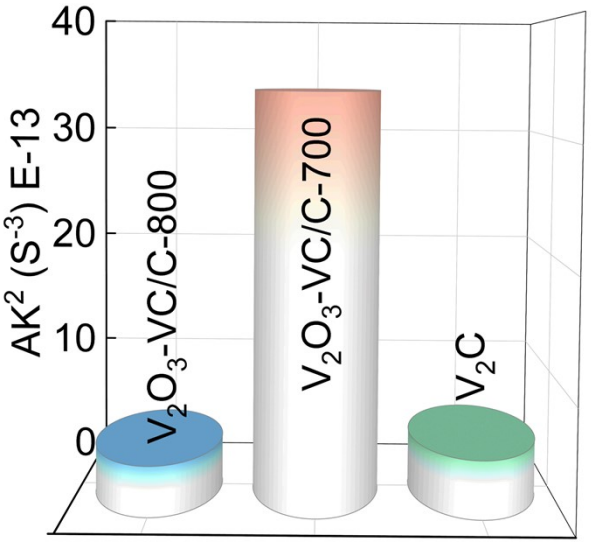

Fig. S10 Nucleation rates of Li_2S with different electrodes.

The nucleation rate constant, growth rate and peak current corresponding to the deposition time of Li_2S are shown in the following equation:

$$AK^2 = \frac{1}{\pi t_m^3} \qquad \text{eq 7}$$

Here, A represents the nucleation rate constant (cm^{-2} s^{-1}), k is the growth rate (cm^{-2} s^{-1}), and t_m is the peak current time (s). The calculated nucleation and growth rate results of Li_2S (Ak^2) are shown in Fig. S10.

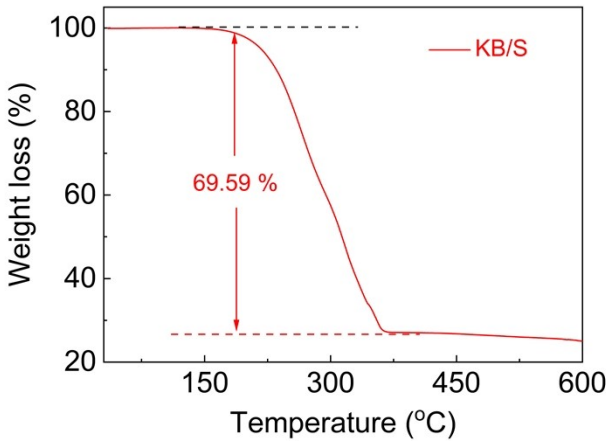

Fig. S11 TG plot of the KB/S composite.

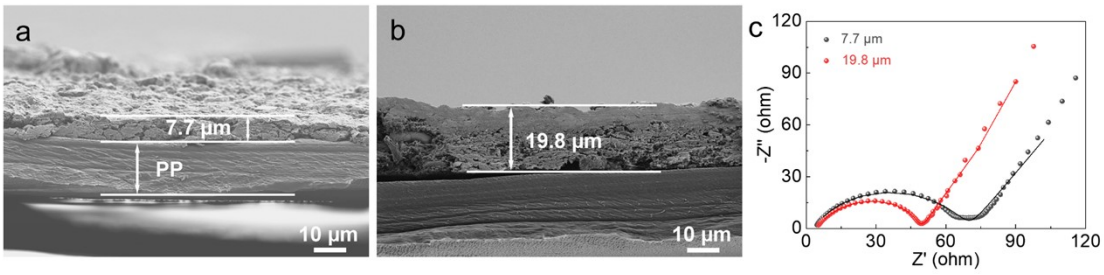

Fig. S12 (a, b) FE-SEM images of the modified PP separators with different coating thicknesses of V_2O_3-VC/C-700. (c) EIS profiles and corresponding fitted data by using the equivalent circuit.

V_2O_3-VC/C-700 modified material was employed to further investigate the effect of different coating thicknesses on the performance of LSBs (Fig. 3h, Fig. S12, and Table S3). As clearly observed from Table S3, the charge-transfer resistance (R_{ct}) of the modified separator is significantly lower than that of the pristine PP separator, indicating that it can effectively optimize the electrode–electrolyte interface, reduce charge-transfer resistance, and accelerate the redox reaction kinetics of LiPSs, thereby improving the reaction kinetics and electrochemical stability of the battery. For the modified separators, R_{ct} shows a decreasing trend with the reduction of coating thickness. Nevertheless, the variation in R_{ct} is negligible when the coating thickness is reduced from 14.2 μm to 7.7 μm. Therefore, to achieve better ion transport and effective suppression of the shuttle effect, the modified separator with a coating thickness of 14.2 μm was used as the main research subject in this work.

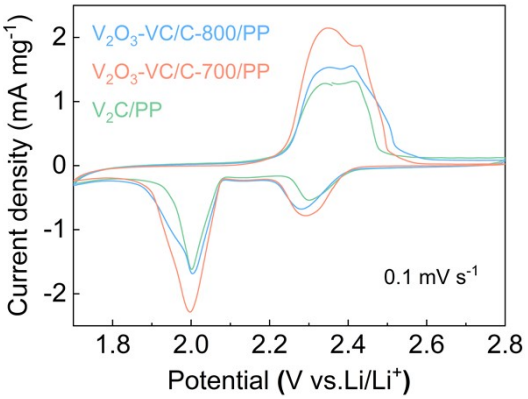

Fig. S13 CV curves (0.1 mV s^{-1}) of V_2O_3-VC/C-800/PP, V_2O_3-VC/C-700/PP and V_2C/PP.

It can be easily observed from Fig. S13 that V_2O_3-VC/C-700/PP provides a higher peak current density than other materials, indicating that its catalytic ability in the LiPS conversion process is superior. This promotes more active materials to participate in the battery reaction, thereby improving the utilization rate of sulfur.

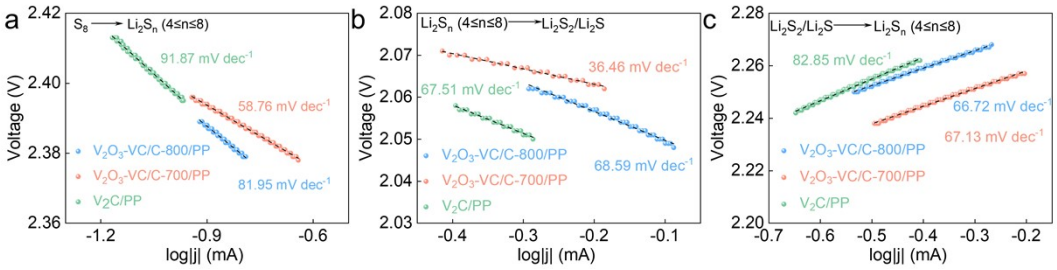

Fig. S14 Tafel plots derived from a) Peak I, b) Peak II, and c) Peak III with different separators.

The Tafel fitting curves intuitively quantify the catalytic behaviors of different modified separators on the LiPSs bi-directional conversion in LSBs. The V_2O_3-VC/C-700/PP based cell exhibits considerably smaller Tafel slope across all three reaction stages than the V_2C/PP and V_2O_3-VC/C-800/PP based cells, reflecting its faster reaction kinetics for LiPSs conversion.

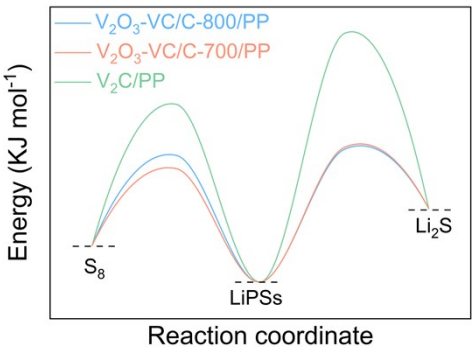

Fig. S15 Activation energies of the reduction conversion of LiPSs.

According to the activation energies of the stepwise sulfur conversion calculated from CV and Tafel data, V_2O_3-VC/C-700/PP based cells illustrate the lowest activation energy for sulfur reduction reaction, further confirming the superior catalytic effect of the V_2O_3-VC/C-700 catalyst.

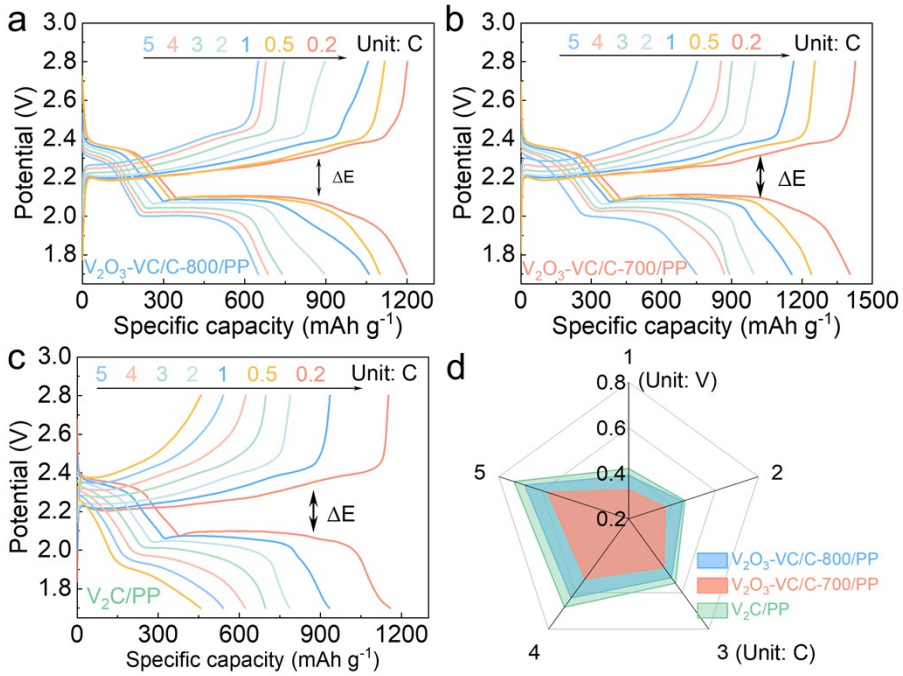

Fig. S16 Charge-discharge curves of LSBs assembled with (a) V_2O_3-VC/C-800/PP, (b) V_2O_3-VC/C-700/PP and (c) V_2C/PP at different current densities, (d) potential difference of the charge-discharge platform.

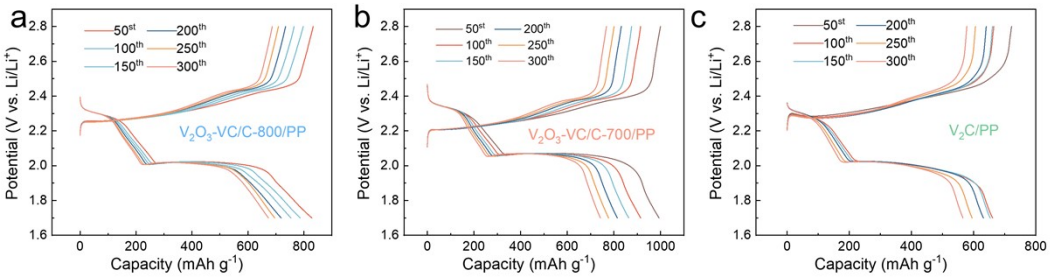

Fig. S17 Charge-discharge curves of LSBs assembled with (a) V_2O_3-VC/C-800/PP, (b) V_2O_3-VC/C-700/PP and (c) V_2C/PP at a current density of 1 C with different cycle.

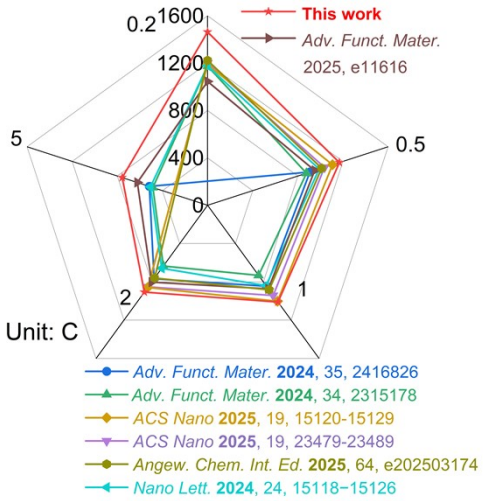

Fig. S18 Comparison in electrochemical performance of V_2O_3-VC/C-700/PP with other recent relevant literature.[6–12]

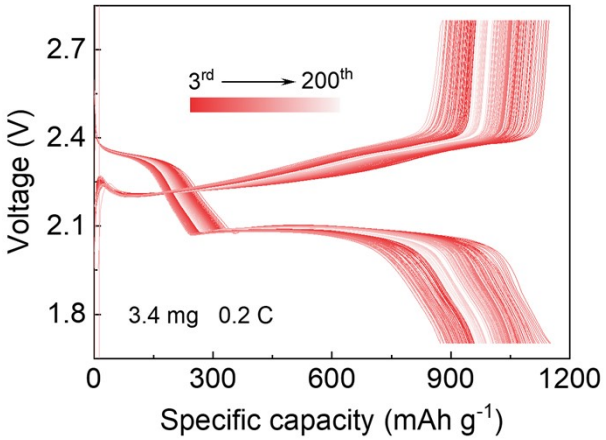

Fig. S19 The charge-discharge plots of V_2O_3-VC/C-700/PP based cell at different cycles.

Table S1 BET specific surface area and pore volume of different materials.

Materials	BET (m^2 g^{-1})	BJH (cm^3 g^{-1})
V_2C	8.722	0.017
V_2O_3-VC/C-700	41.614	0.044
V_2O_3-VC/C-800	17.95	0.042

Table S2 Nucleation and dissolution peak current, the corresponding time and deposition capacity of Li_2S on different electrodes.

	Materials	Current (mA)	Time (s)	specific capacity (mAh g^{-1})
Li_2S Nucleation	V_2O_3-VC/C-700	0.203	4549	237.1
	V_2O_3-VC/C-800	0.085	8740	197.9
	V_2C	0.067	9175	72.4
Li_2S Decomposition	V_2O_3-VC/C-700	0.273	1354	——
	V_2O_3-VC/C-800	0.241	2085	——
	V_2C	0.255	2739	——

Table S3 R_s and R_{ct} for the separators with different coating thicknesses.

Separator	Thickness (μm)	R_s	R_{ct}
PP	0	3.34	86.81
V_2O_3-VC/C-700/PP	7.7	4.81	45.31
V_2O_3-VC/C-700/PP	14.2	3.56	47.83
V_2O_3-VC/C-700/PP	19.8	3.44	63.27

Table S4 R_s and R_{ct} for the different separators as indicated.

Separator	R_s	R_{ct}
PP	3.34	86.81
V_2C/PP	3.64	78.08
V_2O_3-VC/C-700/PP	3.56	47.83
V_2O_3-VC/C-800/PP	3.89	54.93

Table S5 Performance comparison of LSBs with various separators.

Coated Materials	Current rate (C)	Cvcle number	Capacity decay per cycle (%)	*Ref.*
V_2O_3-VC/C-700/PP	**5**	**1500**	**0.034**	**This work**
CoO-Co_3O_4/PP	5	1000	0.065	2
FeCoNiMnRu/CNF	1	500	0.060	13
RP-BP@G/PP	1	500	0.068	14
W/Sn@PP	2	1000	0.060	15
P-MoO_{2-x}/NPC	0.5	1000	0.062	16
Cs_2SnI_6	2	500	0.068	17
V_2CT_x/PCNF	1	400	0.073	18
TCM-50	2	1000	0.057	19
MoB	4	600	0.065	20

Table S6 Performance comparison of LSBs under high-load and low-E/S-ratio conditions.

Materials	Sulfur loading	E/S ratio (μl mg^{-1})	Initial specific capacity (mAh g^{-1}) @ rates	Ref.
V_2O_3-VC/C-700/PP	**3.4**	**14.7**	**1152.2@0.2 C**	**This work**
Fe-ZIF-8	5.0	5.0	517@0.05 C	21
Co-HTP/CG	4.1	--	757@0.2 C	22
Co@SNC	4.1	6	814@0.2 C	23
VC-1/PP	5.3	7	703@0.2 C	24

Reference

1 D. Wang, Z. Dong, H. Yan, X. Lu, C. Shi, F. Liu, L. Huang and Z. Sun, *Adv. Energy Mater.*, 2025, **15**, e04046.

2 M. Zhang, H. Xiao, Y. Liu, W. Hou, X. Li, J. Deng, L. Hou and C. Yuan, *Adv. Funct. Mater.*, 2026, **36**, e20708.

3 W. Hua, H. Li, C. Pei, J. Xia, Y. Sun, C. Zhang, W. Lv, Y. Tao, Y. Jiao, B. Zhang, S. Qiao, Y. Wan and Q. Yang, *Adv. Mater.*, 2021, **33**, 2101006.

4 H. Shi, C. J. Zhang, P. Lu, Y. Dong, P. Wen and Z.-S. Wu, *ACS Nano*, 2019, **13**, 14308–14318.

5 R. Huang, R. Lin, A. Ren, F. Zhao, C. Zhao, R. Sun, X. Yang and X. Gao, *Electrochim. Acta*, 2026, **551**, 148187.

6 Z. Liu, A. Chen, G. Zhang, P. Yu, D. Wang, L. Zhang, K. Tao, F. Han, W. He, Q. Jin, C. Zhang, X. Ma, X. Wang, T. Qi, Z. Li, J. Bai, L. Li, Z. Zhang, J. Dong, J. Li, X. Zhang and L. Wu, *Adv. Funct. Mater.*, 2025, **35**, e11616.

7 L. Sun, H. Xu, J. Xie, Y. Yuan, H. Wang, M. Wang, X. Chen and Z. Jin, *Adv. Funct. Mater.*, 2024, **35**, 2416826.

8 Z. Wang, H. Jiang, C. Wei, K. Tian, Y. Li, X. Zhang, S. Xiong, C. Zhang and J. Feng, *Adv. Funct. Mater.*, 2024, **34**, 2315178.

9 B. Wang, Z. Xing, S. Jia, Q. He, Y. Zhao, X. Meng and S. Tang, *ACS Nano*, 2025, **19**, 15120–15129.

10 R. Zhu, Z. Wu, C. He, S. Li, X. Liu, M. Wu, M. Wang, R. Yan and S. Li, *ACS Nano*, 2025, **19**, 23479–23489.

11 M. Li, H. Liu, H. Li, D. Luan, Z. Liu and X. W. (David) Lou, *Angew. Chem. Int. Ed.*, 2025, **64**, e202503174.

12 H. Ding, Z. Chen, H. Li, H. Suo, C. Liu, H. Yu, J. Yuan, Z. Sun, Y. Zhu and B. Song, *Nano Lett.*, 2024, **24**, 15118–15126.

13 B. Li, H. Wang, Y. Shen, Z. Zhang, Y. Xiong, M. Wang, W. Li, W. Zhou and J. He, *ACS Nano*, 2025, **19**, 12021–12032.

14 X. Dong, X. Chen, X. Tong, G. Liu, H. Yu, W. Liu, H. Li, J. Sun, X. Gu and S.

Zhang, *Chem. Eng. J.*, 2025, **519**, 164704.

15 H. Lu, Y. Su, X. Zhang, Y. Ma, C. Li, S. Luo, L. Kong and Y. Yuan, *Adv. Funct. Mater.*, **35**, 2425863.

16 M. Shi, X. Han, W. Qu, M. Jiang, Q. Li, F. Jiang, X. Xu, S. Ifuku, C. Zhang, C. Wang, J. Hu, L. Yang, Y. Lin, H. Yu, S. Liu, J. Li, Y. Wu and W. Chen, *Adv. Mater.*, 2025, **37**, 2419918.

17 H. Fang, W. Hou, C. Li, S. Li, F. Chu, X. Li, X. Zhang, L. Hou, C. Yuan and Y. Ma, *Chem. Sci.*, 2025, **16**, 8487-8500.

18 S. Jeong, S. Kim, H. Kim, Y. Kim, H. Yu, H. S. Kim and D. Lee, *Small Struct.*, 2025, **6,** 2500277.

19 B. Zhao, L. Song, Z. Zou, Z. Xiong, Y. Zhang, Q. Yang, Z. Shi, Y. Zhang and Y. Song, *Adv. Funct. Mater.*, 2025, **37**, 2500079.

20 J. Pu, S. Fan, Z. Shen, J. Yin, Y. Tan, K. Zhang, B. Wu, G. Hong and Y. Yao, *Adv. Funct. Mater.*, 2025, **35**, 2424215.

21 R. Razaq, M. M. U. Din, D. R. Småbråten, V. Eyupoglu, S. Janakiram, T. O. Sunde, N. Allahgoli, D. Rettenwander and L. Deng, *Adv. Energy Mater.*, 2023, **14**, 2302897.

22 Q. Lv, Y. Sun, B. Li, C. Li, Q. Zhang and L. Wang, *Adv. Energy Mater.*, 2024, **15**, 2403223.

23 Y. Sun, Y. Wang, C. Li, Q. Zhang, L. Wang, Q. Lv and S. Feng, *Adv. Funct. Mater.*, 2025, **35**, 2421780.

24 L. Chen, Y. Sun, X. Wei, L. Song, G. Tao, X. Cao, D. Wang, G. Zhou and Y. Song, *Adv. Mater.*, 2023, **35**, 2300771.